PHYSICAL REVIEW D VOLUME 13, NUMBER 3 1 FEBRUARY 1976

Neutron-proton forward elastic scattering from 58 to 391 MeV*

A. J. Bersbach† and R. E. Mischke‡
Joseph Henry Laboratories, Princeton University, Princeton, New Jersey 08540

T. J. Devlin
Physics Department, Rutgers—The State University, New Brunswick, New Jersey 08903

(Received 15 May 1975)

Elastic neutron-proton differential cross sections have been measured between 58 and 391 MeV incident neutron energy at angles in the center-of-mass system from 11° to 54°. Neutrons were scattered from a liquid-H_2 target and detected in liquid scintillators. The incident energy of each detected neutron was determined from its time of flight. The data were normalized by placing the detector in the beam. The results are generally consistent with previous data and with the predictions of phase-shift analysis but are of improved accuracy.

I. INTRODUCTION

In the last decade a large experimental effort has led to the determination of the main outlines of the *N*-*N* scattering matrix up to about 500 MeV (see Ref. 1) but there are still ambiguities and regions of large uncertainty.[1-3] These lie primarily among the isosinglet phases since the *n*-*p* data are markedly inferior to the *p*-*p* data both in accuracy and in completeness. The differential cross-section data (Fig. 1), which make up most of the *n*-*p* data, are incomplete at c.m. angles below 50° where the low-energy recoil proton is difficult to detect. Below 140 MeV the data appear quite extensive[4-8] but this is mostly due to a single experiment[5] the accuracy of which has been questioned by phase-shift analysts seeking to explain the ambiguity in 50 MeV single-energy solutions. Above 140 MeV the data are few,[9-13] uncertainties are large, and phase-shift results predict forward differential cross sections only to 25%.[14] We report here new and more accurate absolute *n*-*p* differential cross-section data which provide a check on previous data below 140 MeV and substantially improve the data at higher energies.

II. EXPERIMENTAL DETAILS

A. General description

A neutron beam was produced by interaction of the 3.0 GeV proton beam of the Princeton-Pennsylvania Accelerator (PPA) with an internal Pt target. It traversed a liquid hydrogen (LH_2) target and a fraction of the scattered neutrons were detected in scintillation counters. The position of the counters was varied to cover the entire angular range and to enable normalization of the data by measurement of the neutron beam intensity. The incident energy of the neutron in each event was determined by measuring the time between its production by the pulsed proton beam and its detection in the scintillators. The beam had a broad energy spectrum and data were taken simultaneously over the entire energy range.

Laboratory differential cross sections were calculated from

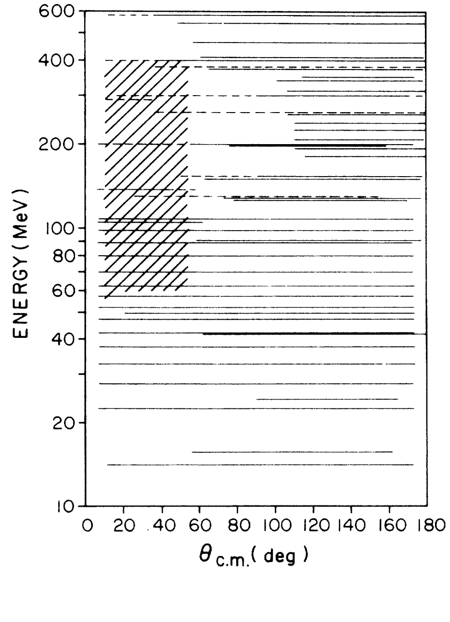

FIG. 1. Extent of *n*-*p* differential cross-section data between 10 and 600 MeV. From the compilation of MacGregor, Arndt, and Wright (Ref. 1) with the addition of the data of Refs. 4 and 22. Solid lines indicate uncertainty < 10%; dashed lines indicate uncertainty > 10%; cross-hashed area is this experiment.

$$\frac{d\sigma}{d\Omega}=\frac{1}{pl\Omega}\,\frac{\phi_s/e_s}{\phi_b/e_b}$$

and

ϕ_s = the scattered neutron intensity (events/monitor count)

$$=\phi_f-\phi_e\,,$$

where ϕ_f, ϕ_e, and ϕ_b are the intensities of neutral events detected in target full, target empty, and beam runs, respectively, ρ is the density of protons in the LH_2, l is the LH_2 target length, Ω is the solid angle subtended at the LH_2 target by the portion of the detector in which ϕ_s was detected, e_s is the detection efficiency for the scattered neutrons, and e_b is the detection efficiency for the beam neutrons. Only the ratio of e_s to e_b appears, so only relative efficiencies are required.

To first order,

$$e_s=e_b$$

since scattered and beam neutrons are nearly indistinguishable near the beam. Also,

$$\phi_f=N_f/M_f\,,$$

where N_f is the number of neutral events detected in a target full run which had M_f monitor counts. Similar expressions hold for ϕ_e and ϕ_b. To this approximation

$$\frac{d\sigma}{d\Omega}=\frac{1}{\rho l\Omega}\,\frac{N_f/M_f-N_e/M_e}{N_b/M_b}\,.$$

A number of refinements to this first-order treatment are outlined in Sec. IV.

B. Synchrotron and T_0

The PPA accelerated approximately 2×10^{10} protons during each 50 msec magnet cycle. The four rf cavities operated at about 30 MHz, the eighth harmonic of the proton orbital frequency. As a result there were eight phase-stable regions, called buckets, in which bunches of accelerated protons circulated around the ring. The time width of the protons from any bunch striking the production target was about 1.1 nsec full width at half maximum (FWHM).[15]

The production time of secondaries was determined with a Lucite Cherenkov counter placed near the production target. Its output was gated with a synchrotron timing signal to reduce noise. The result was a series of pulses called T_0 at intervals equal to the time interval between proton bunches (T_p). Normally T_p was only 33 nsec, the period of the accelerator rf. When T_0 was used as the starting point in a TOF measurement the result was not unique because T_0 was periodic. For many experiments, including this one, the resulting energy ambiguity was difficult to resolve. Consequently, the synchrotron injector was provided with an electrostatic deflection system which prevented injection of protons into selected buckets. Injection into alternate buckets increased T_p to 67 nsec and was referred to as single-chopped injection. Injection into every fourth bucket increased T_p to 134 nsec and was called double-chopped injection. Injection into a single bucket gave a T_p of 268 nsec and was called triple-chopped injection. The deflection system usually permitted less than 0.1% of the beam to enter "empty" buckets. This level of contamination was negligible.

In this experiment the energy ambiguity caused by the periodicity of T_0 was resolved by applying an off-line pulse-height threshold. Neutrons, called ghosts, with any but the highest of the energies possible at a given apparent TOF were rejected by this pulse-height cut. This restricted the energy range of the experiment to a value determined by T_p. If T_p were increased the energy range became greater as lower energies became unambiguously measurable.

C. Neutron beam, LH_2 target, and monitors

The neutron beam (Fig. 2) was taken at 90° with respect to the internal proton beam from the Pt target which was 3.81 cm long, 1.27 cm wide, and 0.63 cm high. The limiting collimator was nested brass tubing 91 cm long. Its defining aperture was 4.84 m from the production target. Two more collimators reduced the background from scattering of neutrons by the primary collimator to the low level necessary for detecting forward scattered neutrons. These were a 5.72-cm diameter steel collimator 1.52 m long and an 11.4-cm diameter, 61-cm long Cu tube embedded in a Pb block of equal length.

The LH_2 target (Fig. 3) was located with its center 8.72 m from the production target. A Mylar flask 7.6 cm in diameter and 68.6 cm long contained the LH_2. The flask was insulated with 25 layers of 6.3-μm aluminized Mylar and enclosed in a 12.7-cm diameter vacuum jacket of 1.32-mm Al. The beam entered the upstream end of the vacuum jacket through an 0.19-mm Mylar window. The assembly was supported and filled at the upstream end to keep downstream material to a minimum.

A Pb plate 5.1 cm thick covered the beam solid angle near the production target and absorbed 95% of the γ's in the beam. Sweeping magnets were located between the production target and

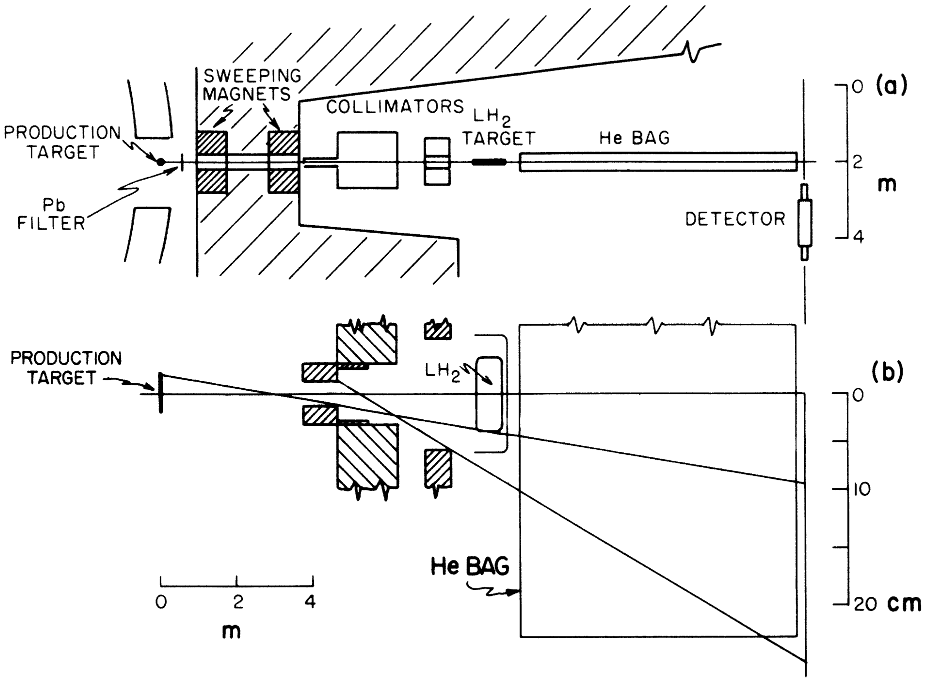

FIG. 2. (a) Plan view of the experimental area; (b) details of the beam geometry showing limiting rays from the production target and the lip of the primary collimator.

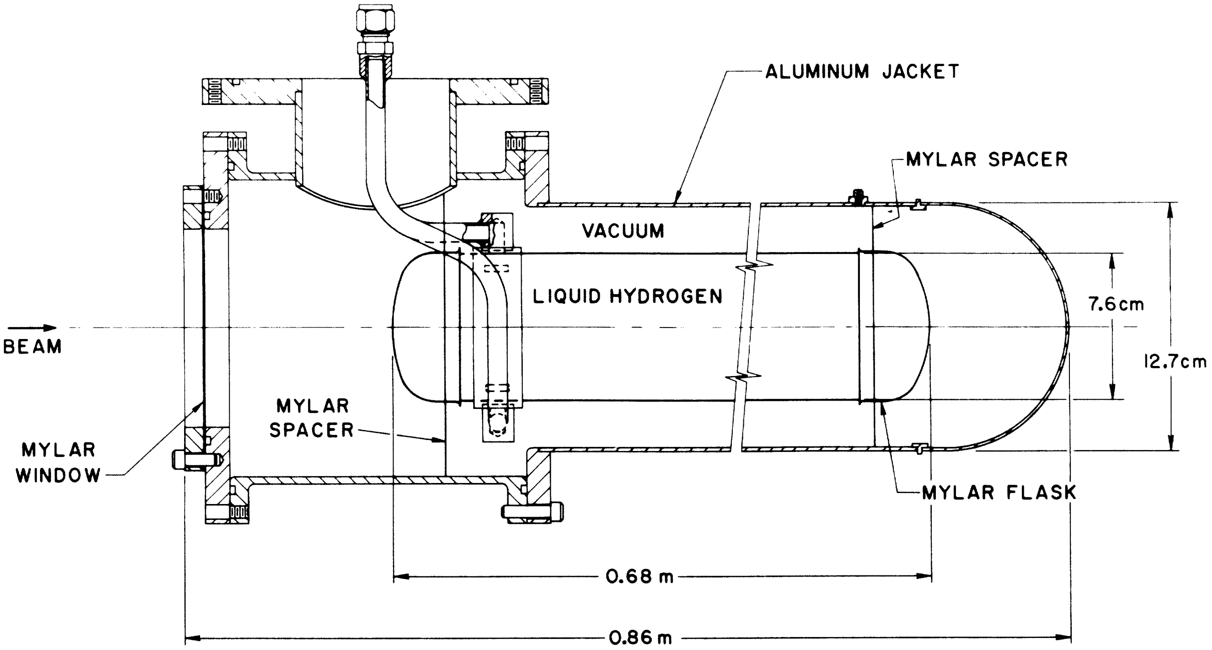

FIG. 3. Schematic of the liquid-H_2 target.

the limiting collimator. A long polyethylene bag with 0.12-mm Mylar entrance and exit windows was filled with He gas and placed downstream of the LH_2 target to reduce scattering from the unscattered beam. The beam was stopped by concrete blocks about 10 m downstream from the detector.

The horizontal beam profile was measured at the LH_2 target and both horizontal and vertical profiles were taken 17.1 m from the production target, where the detector was located. The profiles were in good agreement with those predicted on the basis of beam geometry. The beam at the detector was 10 cm high and 18 cm wide at 5% maximum.

The number of K_L mesons reaching the detector was less than 1% of the number of neutrons reaching the detector in the same TOF bin. The total number of inelastic n-p interactions was less than 5% of the number of elastic interactions in the least populous energy bin used in the experiment.[16] Polarization of the beam was assumed negligible.

The primary beam monitor was a charged-particle telescope located inside the synchrotron ring at the production target. Its counting rate was between 3 and 4 counts per 10^{10} protons onto the production target. A second monitor was a scintillator telescope located in another neutral secondary beam. Its rate was 3 times that of the primary monitor but it was periodically affected by the work of another experiment. It was used only to check the primary monitor except for beam runs when the counts of both monitors were added to improve monitor statistics. The monitors agreed to ± 3%.

D. Neutron detector

The neutron detector (Fig. 4) was composed of three identical neutron counters and surrounding anticoincidence counters on a movable table. The counters were supported from downstream by a steel frame. The table rolled in a pair of Al channel rails which were perpendicular to the beam and extended across it so the detector could be placed in the beam or to either side of it. The table could be raised and lowered so most of the area of the detector face could be placed in the beam.

The neutron counters (Fig. 5) were rectangular boxes made of 1.27-cm Lucite with inside dimensions $120 \times 30 \times 15$ cm^3 covered with a layer of Al foil and two layers of black plastic tape. Their long axes were perpendicular to the beam and their 120×15 cm^2 sides faced upstream toward the LH_2 target. Each was filled with a mineral-oil-based liquid scintillator which was viewed by two Amperex XP1040 photomultipliers, one at

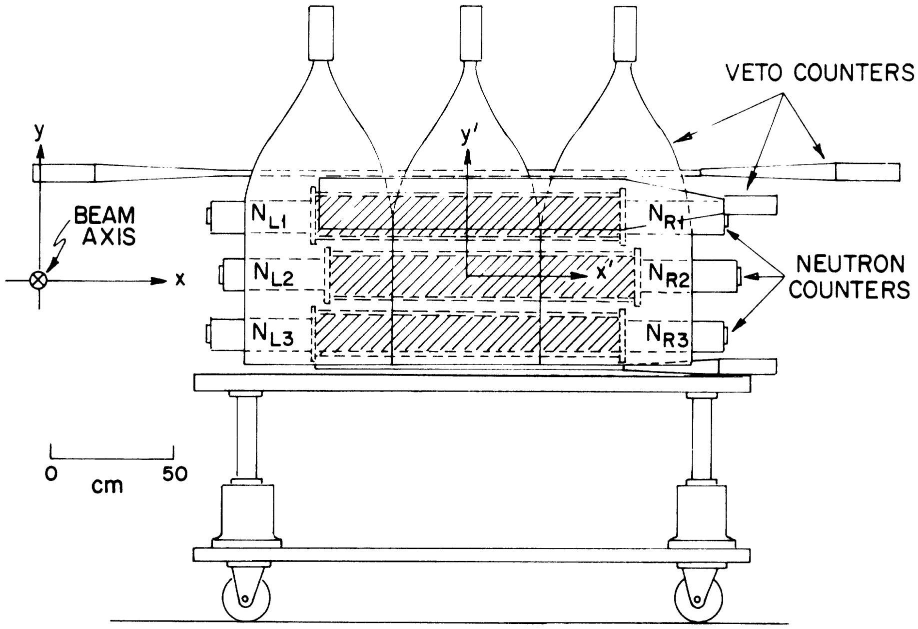

FIG. 4. Schematic of the detector assembly.

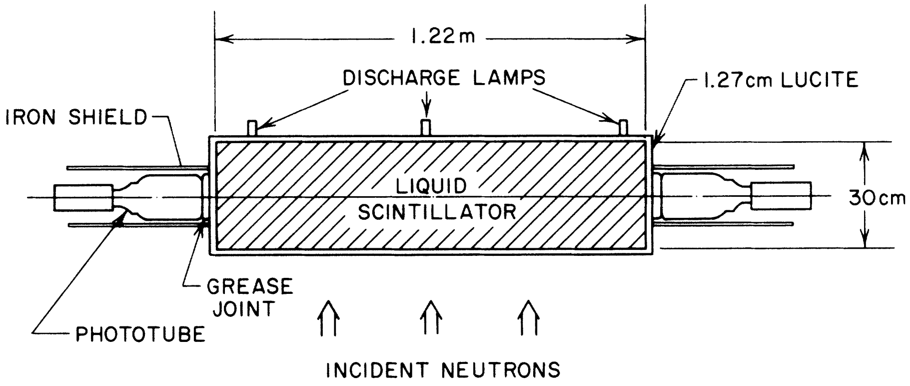

FIG. 5. Schematic of a neutron counter.

each of the 30×15 cm^2 ends. Each photomultiplier was designated N_{ij} where j was 1, 2, or 3 and indicated which of the three scintillators it viewed and i was L or R as the photomultiplier was at the left or right end of the neutron counter viewed from upstream. Argon discharge lamps used to monitor the N_{ij} gains and the position calibration were installed along the downstream face of each neutron counter.

Four anticoincidence counters, each 6.35 mm thick, covered the upstream face of the detector to reject events due to protons scattered from the LH$_2$ target. Four additional anticoincidence counters were placed above and below the neutron counters to reject cosmic rays. The cosmic-ray rejection, which was limited because the anticoincidence counters did not completely cover the detector, was increased to more than 90% by the requirement that scintillations for any event be detected in only one neutron counter (Sec. IIE).

The voltages of the N_{ij} were set so the on-line pulse-height threshold accepted all events of potential interest. Voltages for double-chopped injection were about 100 V higher than those for single-chopped injection. The anticoincidence counters (A_K) were operated about 200 V above the plateau voltage for minimum ionizing particles. The anticoincidence singles rate was about 1000 counts/sec. All photomultiplier voltages were checked regularly and were found to drift less than 0.1% during the experiment.

E. Electronic apparatus

A schematic of the electronic apparatus is shown in Fig. 6. The symbols used there and in the following discussion refer either to the indicated circuits or to their output signals depending on the context. Data were digitized from all events in which signals from both photomultipliers in at least one neutron counter coincided.

Signals from N_{ij} were required to have 600 mV amplitude to trigger discriminator H_{ij} but were timed from 300 mV by discriminator L_{ij} to reduce the pulse-height dependence of the timing. Coincidence Q_1 selected a T_0 pulse to compare with T_L and T_R to provide TOF information. Coincidence Q_2 insured that the selected pulse had T_0 timing. A neutron-counter veto signal, A_N, was generated whenever any three of the L_{ij} coincided, labeling events with signals from more than one neutron counter. The A_K were discriminated and combined with A_N to form a master veto

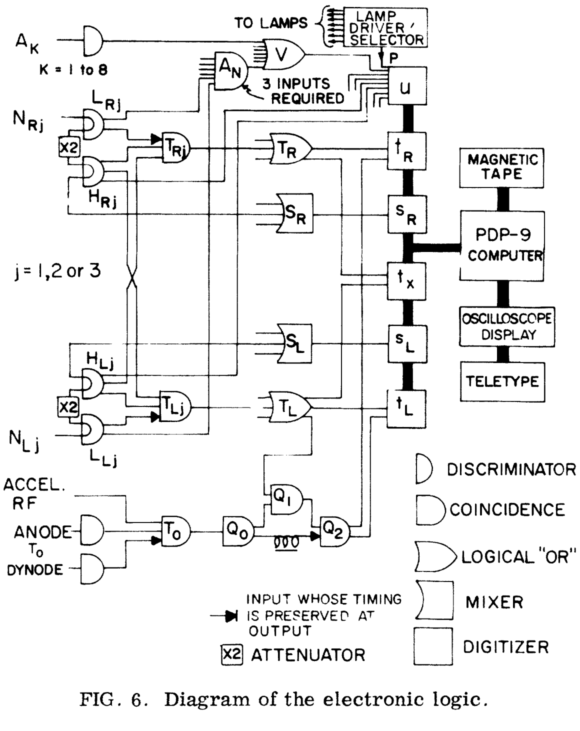

FIG. 6. Diagram of the electronic logic.

signal at V. The discharge lamp system produced a signal called P to label events due to the lamps.

Six pieces of information were digitized and transmitted to a PDP-9 computer when T_L triggered the digitizers and their interface with the computer. These were the following: t_L, the time interval between T_L and T_0; t_R, the time interval between T_R and T_0; t_X, the time interval between T_L and T_R; s_L, the integrated pulse height of S_L; s_R, the integrated pulse height of S_R; and u, an 8-bit latch which recorded the presence of any of V, P, or the H_{ij}. All events without V were recorded on magnetic tape by the computer. In addition, one vetoed event in 32 was recorded for diagnostic purposes.

The cosmic-ray contamination of the data was reduced to a minimum by permitting data to be taken only when the beam flux indicated by integrating T_0 exceeded a minimum value. The data taking was also gated by synchrotron timing signals, by a dead-time trigger initiated by T_L, by busy signals from the computer interface, and by a gate preceding each discharge lamp event which increased the acceptance of lamp events during beam runs.

In addition to supervising the recording of the data the computer provided on-line displays of a number of quantities. These displays were extremely useful for tuning and for diagnosis of apparatus malfunctions.

F. Data taken

A total of 122 runs were taken during this experiment. Of these, 80 recorded data from scattered neutrons. In a typical scattering run 5000 vetoed and 50 000 unvetoed events were recorded. Forty such runs were taken with single-chopped injection giving cross-section data down to 130 MeV. Three beam runs taken with double-chopped injection gave information on the ghost contamination of these data. The other 40 scattering runs were taken with double-chopped injection and increased photomultiplier voltages enabling cross-section measurements to 58 MeV. Three beam runs taken with triple-chopped injection gave information on ghost contamination of these data. Of the remaining runs, 29 were taken with the detector in the beam to obtain normalization and 7 were taken with the beam off to measure the cosmic-ray background.

III. RECONSTRUCTION

A. Latch

The first step in the off-line reconstruction was the classification of each event on the basis of the latch information (u). The neutron-counter bits were examined to see if those which were set corresponded to both photomultipliers in a single neutron counter. If so, the neutron-counter number, j, was determined. All other events were classified as "invalid" and were not analyzed further. Each of the "valid" events was placed in one of three classes depending on the state of V and P. Events for which V was set were called "vetoed" events, events for which P was set were called "lamp" events, and events for which neither was present were called "neutral" events. The number of events of each class in the final data set is shown in Table I.

Some classes of invalid events violated the online logic and indicated the extent of timing errors and inefficiencies. No events with only one of the H_{ij} should have occurred but 0.1% of the recorded events were of this type. All events for which there were more than two H_{ij} should also have had V due to A_N but less than half of the recorded events with more than two H_{ij} had V. Since only one vetoed event in 32 was recorded this indicated that A_N was about 5% inefficient. Neither of these effects had a significant effect on the results.

B. Time of flight and position

The time-to-digital converters were calibrated by connecting to their "start" and "stop" inputs signals whose time difference was determined by a precision variable delay line. Scale factors for t_L, t_R, and t_X were 8.63, 8.97, and 8.45 channels/nsec, respectively, so least-count error was about 0.06 nsec. The time-to-digital converters were measured to be linear within 0.1 nsec over the range occupied by the data.

The T_L gate had a width somewhat greater than T_p; if no T_0 signal were missing one was sure to be present with T_L at Q_1 and if two or more successive T_0 signals were missing none would be

TABLE I. Disposition of events.

	Single-chopped		Double-chopped	
	Target full	Target empty	Target full	Target empty
Monitor counts	1 446 027	1 103 211	262 655	240 222
Lamp events	134 643	92 346	36 620	36 055
Vetoed events	225 415	65 625	55 696	37 557
Neutral events:				
Valid	775 172	282 068	544 417	230 771
T_L gated	728 205	261 685	510 990	214 188
Above off-line PH threshold	323 685	109 886	290 426	120 936

present. If only one were missing, however, a signal might or might not be present depending on the interval between T_L and T_0 and, therefore, on the TOF and position of the event. The dependence was eliminated off-line by making a cut in t_L which effectively reduced the width of the on-line gate produced by T_L to T_p. The number of events, called "T_L gated" events, surviving this cut is shown in Table I. "Ungated" events were counted as described in Sec. III so the data could be corrected for their loss.

The time of flight, t, and position along the detector, x', were determined for each valid event. Extraction of t and x' from t_L and t_R required determination of electronic propagation times, time slewing, and the velocity of light in the scintillator since

$$t_L = D_{Lj} - D_{T_0} + (x'_{Lj} - x')/c_d + t = C_{Lj} - x'/c_d + t$$

and

$$t_R = D_{Rj} - D_{T_0} + (x' - x'_{Rj})/c_d + t = C_{Rj} + x'/c_d + t\,,$$

where D_{ij} is the time between the arrival at N_{ij} of photons due to an interaction and the arrival of the corresponding T_i signal at the time-to-digital converter, D_{T_0} is the time between the arrival of a proton bunch at the production target and the arrival of the T_0 signal at the time-to-digital converter, x'_{ij} is the x' position of the face of N_{ij}, c_d is the speed of light in the scintillator, and the C_{ij} are constants incorporating the constants in the expressions for t_L and T_R. The D_{ij} and therefore the C_{ij} are functions of pulse height because they include the time required for photomultiplier signals to rise to the 300 mV discrimination level and this time is dependent on pulse height.

The C_{ij} were determined from the t_i for γ rays intersecting the detector at $x' = 0$, using the known TOF, t_g (= 56.9 nsec), of γ rays; $C_{ij} = t_i - t_g$. Each of the C_{ij} was determined for ten different pulse-height bins. These ten values were then fit to a quadratic in the pulse height, s_i, giving $C_{ij}(s_i)$. The quadratic fit fell within 0.1 nsec of nearly all of the experimentally determined values of C_{ij}. The C_{ij} decreased by about 1.5 nsec from the lowest to the highest pulse heights.

For any event, then, the expressions above for t_L and t_R give

$$t = \tfrac{1}{2}[t_L + t_R - C_{Lj}(s_L) - C_{Rj}(s_R)]$$

and

$$x' = \tfrac{1}{2} c_d [t_R - t_L + C_{Lj}(s_L) - C_{Rj}(s_R)]\,,$$

where t is only determined modulo T_p, the period of T_0. The FWHM of the γ peak in the t distribution was 2.0 nsec, a good measure of the over-all TOF resolution.

The value of c_d was determined by causing the beam to intersect the counters at known values of x' and observing the resulting peak in the distribution of $t_R - t_L + C_{Lj}(s_L) - C_{Rj}(s_R) = 2x'/c_d$. The result was 15.8 cm nsec^{-1}, consistent with that determined by Dakin *et al.*[17] With this value of c_d the x' coordinate of the center of the beam which was calculated from the timing data agreed with that determined by geometry to within 1 cm everywhere along the detector. The width of the beam spot determined from the timing data was 15 cm FWHM, consistent with that expected from geometry alone. This indicated the angular resolution of the apparatus including beam divergence and position resolution but not including the effect of the uncertainty in the scattering point within the LH$_2$ target. The x' distributions of discharge lamp events had FWHM of 7 cm. Figure 7 shows typical final TOF and position spectra.

C. Pulse height

The pulse-height information, s_L and s_R, recorded for each event was used to estimate s, the light produced in the scintillator by each event. Before this was done both analog-to-digital converters (ADC's) were calibrated and the relative photomultiplier gains and gain drifts were de-

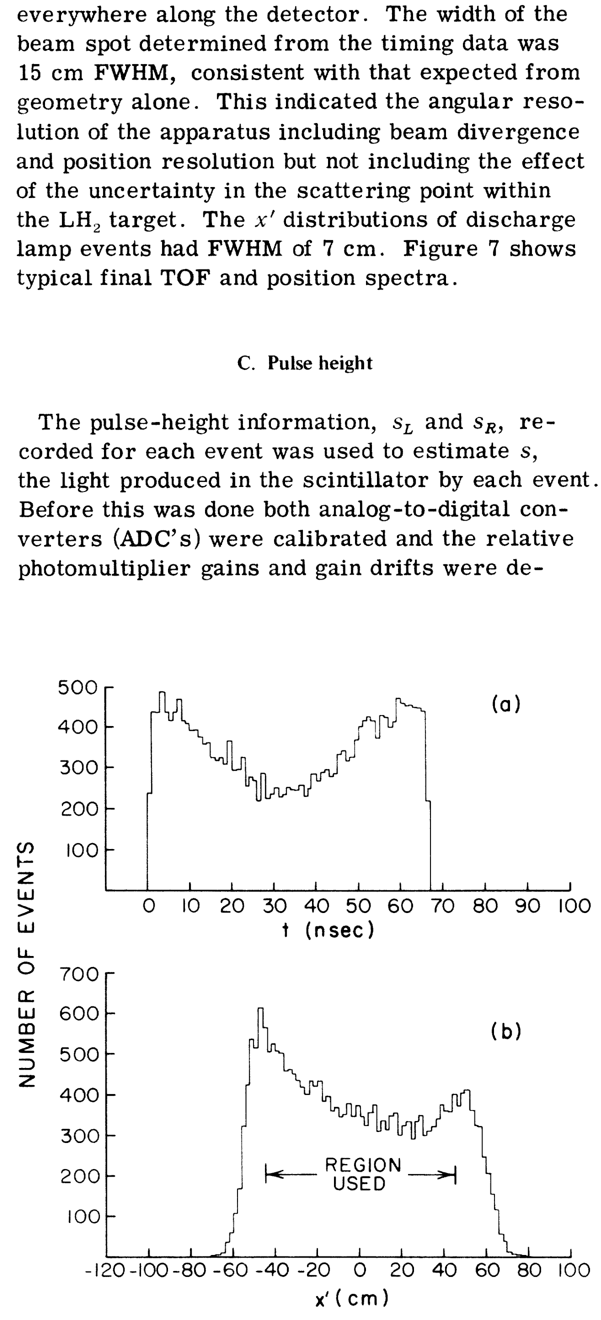

FIG. 7. (a) Typical TOF spectrum; (b) typical position distribution.

termined.

The s_L and s_R ADC's deviated from being linear by less than 3%. The offset of the ADC's was determined by attenuating the signal from a pulse generator by known amounts and extrapolating to zero. Appropriate corrections were made to s_L and s_R.

The gain drift of each neutron-counter photomultiplier was determined by measuring the signals from the Ar discharge lamps. The mean pulse height generated in each of the N_{ij} by each of the three lamps it viewed was determined for every run. The gain $g_{ij}(n)$ of N_{ij} in run n was chosen to match these pulse heights to those in an arbitrarily chosen reference run. The change in g_{ij} was as much as 17% over the course of the experiment but the difference in g_{ij} between the runs of a full-empty pair was never more than 3% and the rms difference was 0.5%.

The gains of the N_{ij} relative to one another were determined from the thresholds required to give the same rate in each under similar conditions. The relative gain G_{ij} for N_{ij} was proportional to the threshold required in N_{ij} to produce a rate which was the same for all the N_{ij} when the threshold was high enough to eliminate the effect of the on-line thresholds. These relative gains were used only to make the x' dependence of the off-line detector efficiencies small enough so x'-independent ghost-reduction thresholds would not unnecessarily reduce the efficiency of any part of the detector. The remaining x' dependence was measured and corrected as described in Sec. IV E.

An independent measure of the gain of each neutron-counter photomultiplier in each full-empty pair was derived from the pulse-height spectra of protons scattered from the LH_2 target by the neutron beam. The g_{ij} so determined differed from those determined with the lamps by 1.5% on the average. The G_{ij} differed from those determined from beam thresholds by less than 4%. These calculations provided light attenuation data for the Monte Carlo neutron-counter efficiency calculations which are described in Sec. IV E.

The total pulse height s was computed for each event by adding the corrected pulse heights (PH) from both photomultipliers in the counter in which the event was detected:

$$s = s_L/[G_{Lj}\,g_{Lj}(n)] + s_R/[G_{Rj}\,g_{Rj}(n)] \; .$$

The normalization of the corrections is such that s is approximately equal to $s_L + s_R$ so that its units, called PH units, are approximately equivalent to ADC channels.

Typical final pulse-height spectra are shown in Fig. 8.

D. Binning

The analysis of each valid event produced three quantities, t, x', and s. The distance r of each event from the beam at the detector was determined from x' and the position of the detector during the run assuming that each event was on the long axis of the counter in which it was detected. The incident energy E was determined from t and r assuming each event was due to a neutron elastically scattered at the center of the LH_2 target.

Bin boundaries were identical for all runs. The range of the experiment in r, 65.8 to 394.1 cm, was divided into 23 bins 15.2 cm in width. Only the 6 bins in each run which were nearest the center of the detector were used in the final analysis. The energy range of the experiment, 55 to 430 MeV, was divided into 20 bins. Only 13 energy bins, those above 120 MeV, were accessible with single-chopped injection.

Binning for each event was carried out for ten pulse-height thresholds at once to allow studies

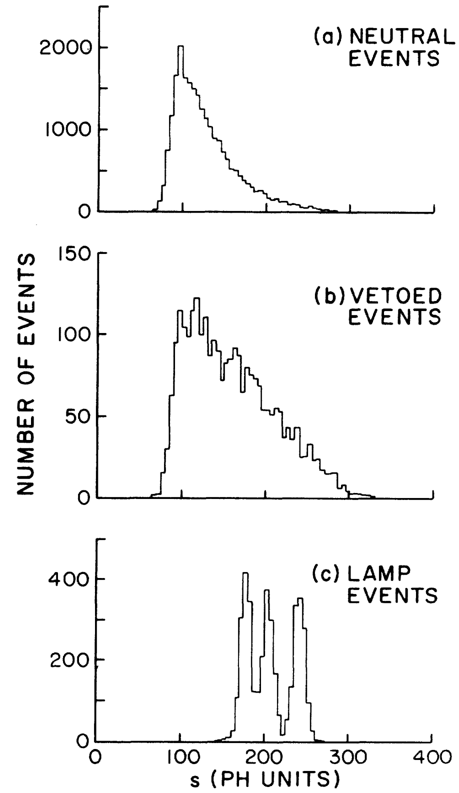

FIG. 8. Typical pulse-height spectra: (a) neutral events; (b) vetoed events; (c) lamp events, showing the peaks due to the three lamps in a single neutron counter.

of threshold dependencies and selection of final thresholds without repeating the reconstruction of each event. Pulse-height thresholds were different for single- and double-chopped injection because the energy difference between "ghost" and "real" neutrons was much greater for double-chopped injection and because photomultiplier voltages were different for the two injection modes.

The primary results of binning a run were $N_m(E, r)$, the number of valid events in bin (E, r), if the run was a scattering run (in which case m was f or e as the target was full or empty), or $N_b(E)$, the number of valid events in energy bin E, if the run was a beam run, or $N_c(r)$, the number of valid events in radial bin r, if the run was a cosmic run.

Several other quantities were determined during binning for use in consistency checks and to correct for the absence of a T_0 signal within the t_L gate: N_N, the total number of valid neutral events above threshold, N_{NG}, the total number of t_L gated neutral events above threshold, N_L, the total number of valid lamp events above threshold, and N_{LG}, the total number of t_L gated lamp events above threshold.

A special procedure was employed for beam runs taken to determine the contamination of the data by ghost neutrons. In these runs the detector photomultipliers were operated with the voltages used in taking data with single- and double-chopped injection while the accelerator was operated with double- or triple-chopped injection, respectively. T_p was, therefore, double the value usual for the photomultiplier gains being used and the ghost neutrons could be resolved by TOF (Fig. 9). The energy bin into which each detected neutron went was that into which it would have gone with normal timing but ghosts were binned in a separate array. Then the ratio of the number of ghost neutrons to "real" neutrons was calculated for each neutron counter for each threshold and energy bin.

IV. ANALYSIS

A. Consistency

Before continuing with the analysis the consistency of the binned data was checked by examining the intensity of scattered neutrons detected in each full-empty pair. The total intensity of neutral events in each run was

$$\Phi_m = N_N/M\ , \quad m = f, e$$

and the intensity of scattered neutrons in a pair was

$$\Phi_s = \Phi_f - \Phi_e\ ,$$

where Φ_f and Φ_e are neutral-event intensities for the full and empty runs of the pair, respectively. Φ_s was plotted as a function of the distance r_c of the center of the detector from the beam (Fig. 10) to enable comparison of data taken at different detector positions. Most of the pairs were consistent but the intensities found for the last 12 pairs were internally inconsistent and higher than those of the other pairs.

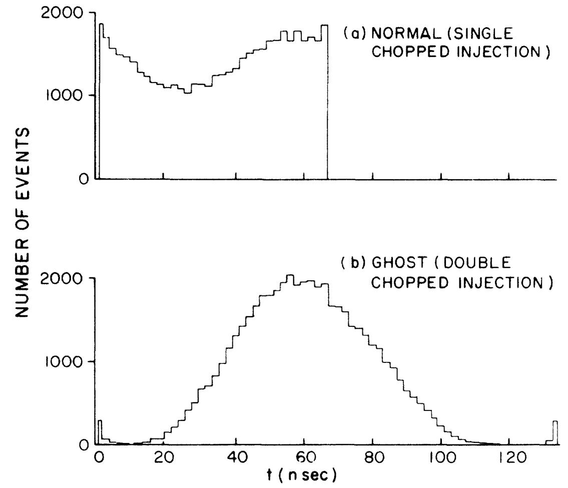

FIG. 9. (a) Beam timing spectrum for single-chopped injection taken with the neutron-counter voltages appropriate to single-chopped injection; (b) beam spectrum for double-chopped injection showing resolution of the TOF ambiguity.

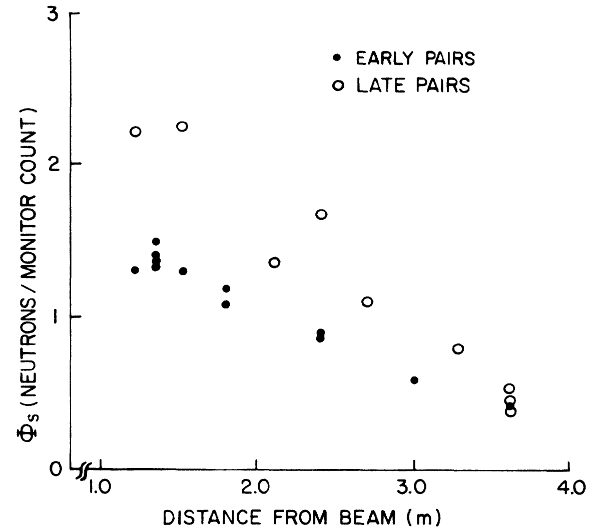

FIG. 10. Neutron intensity in a given full-empty pair vs the distance of the center of the detector from the beam showing the inconsistency of early and late pairs.

Late runs always had greater detected neutron intensities than did identical runs taken early. The differences in pulse height, TOF, and position spectra of two similar runs, one early and one late, were indistinguishable from those of vetoed events and quite different from those of neutral events. The position spectra of neutral events in the later runs showed no pronounced distortion such as would have occurred had the inconsistency been due to failure of mistiming of one of the veto counters. The inconsistency appeared to be due to a change made in the veto electronics at the onset of the inconsistency. Since the early data were quite consistent the problem was resolved by rejecting the late data.

B. Off-line pulse-height thresholds

The off-line pulse-height threshold to be used in each energy bin was selected fron the ten thresholds used in binning by requiring the ghost contamination at that energy to be less than 5%. The ghost contamination used for this purpose was the ratio of "reals" to ghosts determined as described in the last paragraph of Sec. III D. The error in the final results due to this level of ghost contamination was always less than 3%.

C. Cosmic-ray background and T_0 efficiency corrections

For a scattering run the number of events per monitor count in a bin, corrected for T_0 efficiency and for the cosmic-ray background, was

$$\phi_m = (N_m - \phi_c L u_c t_k / T_p)/(u_s M_m),$$

where $\phi_c = N_c/L$ the cosmic-ray background intensity per live-time count; $m = e$ or f as the LH_2 target was empty or full; t_k = the TOF width of the energy bin; u_c = the T_0 efficiency for cosmic-ray events; and u_s = the T_0 efficiency for neutrons scattered from the beam.

The magnitude of u_s was greater than that of u_c because both T_0 and the scattered neutron intensity were correlated with the accelerator beam intensity while the cosmic-ray intensity was independent of the accelerator. The magnitude of u_c was equal to that of u_L, the T_0 efficiency for lamp events, because lamp events were also independent of the accelerator:

$$u_c = u_L = N_{LG}/N_L .$$

The value of u_s was determined from the number of gated and ungated neutral events after subtracting the cosmic-ray contribution. It was found to be consistent with a constant value of 0.97 and this value was assumed in the subsequent analysis.

All scattering runs were corrected for the cosmic-ray background but they were also checked without the cosmic-ray correction. The rms difference in the two sets of results was 3%, so the results are quite insensitive to ϕ_c.

In beam runs the detected neutron intensity exceeded that in scattering runs by a factor of about 10^3 so the cosmic-ray correction was negligible and the equations for the intensity and T_0 efficiency reduce to

$$\phi_c = N_b/(u_s M_b) \text{ and } u_s = N_{NG}/N_N .$$

When N_{NG}/N_N was calculated, however, it was found to be about 0.87, 10% less than that due to T_0 counter inefficiency. This was traced to a delay of about 110 nsec between discriminators T_0 and Q_0. The instantaneous rate during beam runs was about 10^6 sec^{-1} so about 10% of the valid events occurred so soon after the end of the dead time for the previous event that T_0 had not reached Q_1 by the time T_L got there. Consequently, no TOF information was recorded for these events and they did not pass the off-line t_L gate. Correction for the loss of these events could not be carried out as if they were due to T_0 counter inefficiency, however, because the probability that the TOF information would be lost through this mechanism was a function of t_L. Correction of the beam data for events lost by this mechanism was carried out by modifying the beam binning procedure so as to give added weight to events which had a high probability to be lost.

D. Target-empty subtraction

The target-empty subtraction removed the background due to scattering from the target flask and transmission through the shielding around the collimators. The neutron intensity in each bin for the target-empty run of each pair was subtracted from that for the target-full run:

$$\phi_s = \phi_f - \phi_e .$$

The subtracted data from full-empty pairs taken at the same detector position with the same photomultiplier voltages were averaged. Then they were corrected for the r and x' dependence of the detector efficiency as outlined in the next section.

E. Detector-efficiency corrections

The efficiency of the detector for scattered neutrons of a given incident energy with a given pulse-height threshold depended on their final energy, their angle of incidence of the detector face, and their position along the counter in which they were detected. The correction required for each of these effects was small so they were assumed independent and the detected neutron flux was described by

$$\phi_s = \phi(r) h_E(E_f) h_\theta(\theta_f) h_j(x') e_b ,$$

where $\phi(r)$ is the neutron r distribution at the detector due to neutrons of incident energy E_{inc}, $E_f(r)$ is the final energy of such neutrons detected at r, $\theta_f(r)$ is the angle of incidence of such neutrons on the detector face with respect to its normal and is equal to θ_L, the laboratory scattering angle, h_E describes the energy dependence of the detector efficiency near E_{inc} where $h_E(E = E_{\text{inc}}) = 1$, h_θ describes the dependence of the detector efficiency on θ_f near 0° where $h_\theta(\theta = 0) = 1$, and h_j describes the x' dependence of the efficiency of neutron counter j where $h_1(0) = 1$.

The h_j were determined by comparing the response of different parts of the detector to neutrons scattered at the same angle. The detected neutron intensity was expressed as

$$\phi_s = \phi'(r) h_j(x') ,$$

$$\phi'(r) = \phi(r) h_E(E_f(r)) h_\theta(\theta(r)) ,$$

and the h_j were assumed quadratic in x':

$$h_j(x') = a_j + b_j x' + c_j x'^2 .$$

An iterative computer program adjusted ϕ' and the a_j, b_j, and c_j to values which minimized χ^2 calculated using the data for all 11 detector positions with uncertainties due to counting statistics. The values of χ^2 were consistent with those expected from statistics. The values of b_j and c_j were consistent with zero so this was assumed in the subsequent analysis.

The dependence h_E of the efficiency of the detector on neutron energy was determined by a Monte Carlo calculation which simulated neutron-induced events and determined their light output.[18] The program was checked by comparing its results with experimental-beam pulse-height distributions (Fig. 11) and with the detector effective height determined experimentally as described in Sec. IV G. The results indicated that the program accurately represented the detector over the small ranges of neutron angle and energy for which information was needed.

The detection efficiency H_E for neutrons normally incident on the detector face at $x' = 0$ and uniformly distributed in the vertical direction was determined as a function of energy and threshold (Fig. 12). To correct the data in a given energy bin for energy loss in scattering, the data for the ghost-reduction threshold corresponding to that bin were interpolated and used to determine $H_E(E_{\text{inc}})$ and $H_E(E_{f\,\text{min}})$ where $E_{f\,\text{min}}$ is the final energy of neutrons scattered at the largest angle

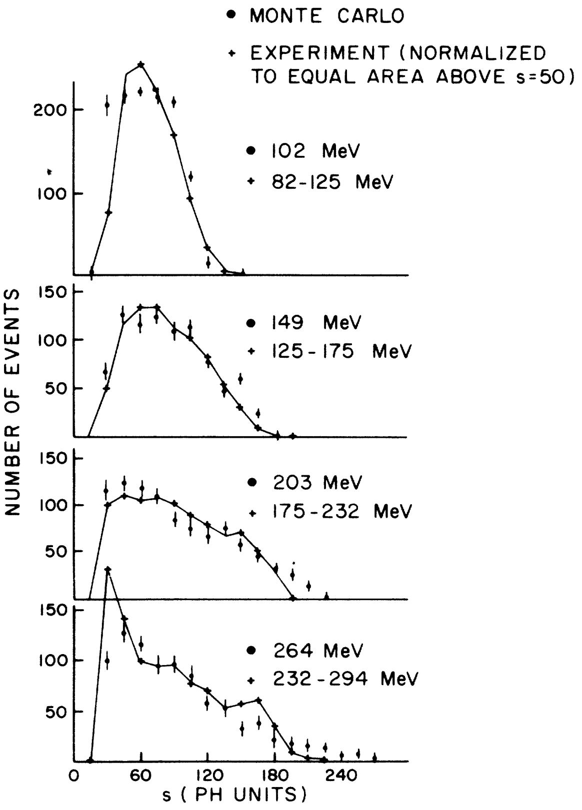

FIG. 11. Comparison of experimental and Monte Carlo pulse-height distributions for neutrons of four energies. The spectra are normalized to equal numbers of events above 50 PH units.

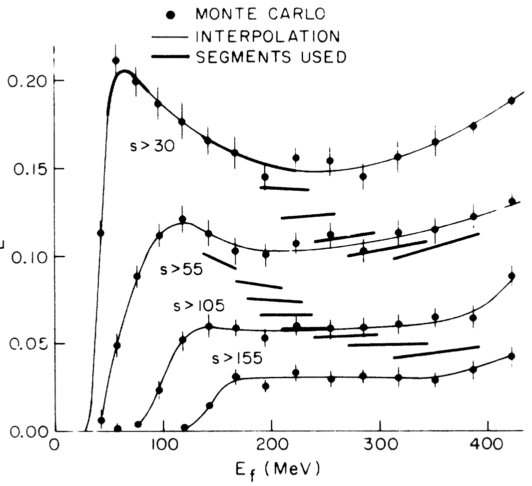

FIG. 12. Detection efficiency vs neutron kinetic energy determined by Monte Carlo calculation for 4 pulse-height thresholds. Heavy lines show efficiencies used in most energy bins for the final analysis.

at which data were taken. For smaller angles H_E was determined by a linear interpolation in E_f so that the efficiencies used fell along the line segments shown in Fig. 12. Finally,

$$h_E(E_f) = H_E(E_f)/H_E(E_{\text{inc}}) .$$

These correction factors differed from unity by 27% at most. It was difficult to calculate their uncertainty because it is hard to predict the effects of the simplifications introduced in the Monte Carlo calculation. A rough estimate was made by taking 30% of $h_E(E_{f\,\text{min}}) - 1$ which was about 5% independent of energy.

The angular dependence of the detection efficiency, h_θ, was assumed proportional to the thickness of scintillator traversed by the scattered neutrons, i.e.,

$$h_\theta(\theta_L) = \sec\theta_L .$$

This assumption is strictly justified only when the dimensions of light-producing events in the detector are much smaller than the neutron path length in the scintillator. This was not generally the case so the $\sec\theta_L$ dependence of the detection efficiency was checked at several energies using the Monte Carlo model of the detector to simulate the detection of neutrons incident on the detector face at a 30° angle. The results were consistent with the assumption within their 5% statistical accuracy. Since θ_L never exceeded 30° its secant was 1.15 at most.

F. Scattering corrections

Scattering processes which modified the neutron intensity detected in a particular segment of the detector can be divided into three classes:

(1) scattering of beam neutrons into the detector segment by material other than LH_2,
(2) scattering away from the segment of neutrons originally directed toward it, and
(3) double scattering of neutrons originally directed elsewhere into the segment being considered.

The effect of these processes was determined by a Monte Carlo simulation.

Events of the first class were almost entirely due to diffractive scattering in He gas.[19] Scattering by material upstream of the LH_2 target canceled in the target-empty subtraction. Scattering in He reduced apparent cross sections since it was reduced when the target was filled. Inelastic scattering by He was swamped by elastic scattering, despite comparable total cross sections, because of the strong forward peaking of elastic events.

Events of the second class were almost entirely due to double scattering in LH_2.[20] Because of the target geometry they, like events of the first class, resulted in a reduction of the apparent differential cross sections whose magnitude was strongly forward peaked.

Events of the third class were usually due to double scattering in the LH_2. The Monte Carlo simulation showed that no more than 3% of the neutrons reaching the detector would have been due to events of this class if the beam had been a monoenergetic beam within the energy range of the experiment. The actual contamination of the data should have been even lower because the TOF of these events classes them with elastic scattering events of lower incident energy and greater final energy. The lower incident energy of the elastically scattered events meant that they came from a higher-intensity portion of the beam-energy spectrum than did the double scattering events. The higher final energy of the elastic events meant that they generally had higher detection probability.

Because it was small and could not be estimated accurately, the effect of double scattering of neutrons into the detector was neglected. Correction for the other two classes of events was carried out using the Monte Carlo simulation to determine ϕ_0, the "observed" neutron intensity at the detector, and ϕ_1, the intensity due to neutrons single scattered by the LH_2, as a function of r at six energies spanning the energy range of the experiment. Correction parameters $A(r,E) = (\phi_1 - \phi_0)/\phi_0$ were determined so that the data could be corrected as follows:

$$\frac{d\sigma}{d\Omega} \rightarrow \frac{d\sigma}{d\Omega}\left[1 + A(r,E)\right] .$$

For convenience, angular factors $A_r(r)$ were determined which gave the best fit to the Monte Carlo $A(r,E)$ at all six energies assuming that $A(r,E) = A_r(r)A_E(E)$ where A_E has the energy dependence of the attenuation of the beam by the LH_2. The original Monte Carlo results and the values of $A(r,E)$ which were derived from this fit and used in correcting the data are shown for three energies in Fig. 13.

The uncertainties in these corrections were negligible except that the neglect of the third class of events may have resulted in overestimates of low-energy cross sections by as much as 2% and the form assumed for the energy dependence of $A(r,E)$ may have underestimated the low-energy cross sections by a like amount.

G. Effective solid angle and normalization

The effective solid angle of a detector segment is the radial bin width multiplied by the effective height of the detector. The effective height Δy was determined experimentally by measuring the response of the detector when the beam was centered on a series of points closely spaced along a vertical line on its face. Δy was found to be 13.8 ± 0.5 cm. It was independent of x' and energy within 10% statistical errors except at the ends of the counters, outside the x' region for which data were accepted.

The experimental value of Δy was checked using the Monte Carlo model of the detector described in Sec. IV E. In this case Δy was determined from

$$\Delta y = \frac{\phi_v \Phi_b}{p_v \phi_b} ,$$

where ϕ_v is the number of neutrons detected when the incident neutrons were uniformly distributed along a vertical line with p_v neutrons per unit length and ϕ_b is the number of neutrons detected of Φ_b neutrons with the geometry of the actual beam when it was centered on a neutron counter. Calculations were carried out for 77, 119, 225, and 343 MeV. The average result was 13.5 cm. There was no apparent dependence on energy or pulse height within the 10% statistical uncertainty.

Normalization of the data was carried out using beam intensities ϕ_b at each energy determined from measurements made at several times during the experiment. The individual measurements were corrected for the relative efficiencies of the counters using the h_j discussed in Sec. IV E. They were averaged to obtain the final results. Beam data taken at the same detector position were checked for consistency. The average over detector position of the rms deviation of such runs from the mean at each position was about 10% and appeared independent of energy. Monitor statistics contributed 5% but no cause could be found for the remaining inconsistency. These relative deviations were adopted as the best estimate of the uncertainty in the normalization. This estimate of the uncertainty in the normalization includes an effect, monitor statistics, which does not contribute to the normalization uncertainty due to the statistical cancellation of monitor statistics for the several runs used in determining the normalization but it does not include the uncertainty in Δy and the two effects have the same magnitude.

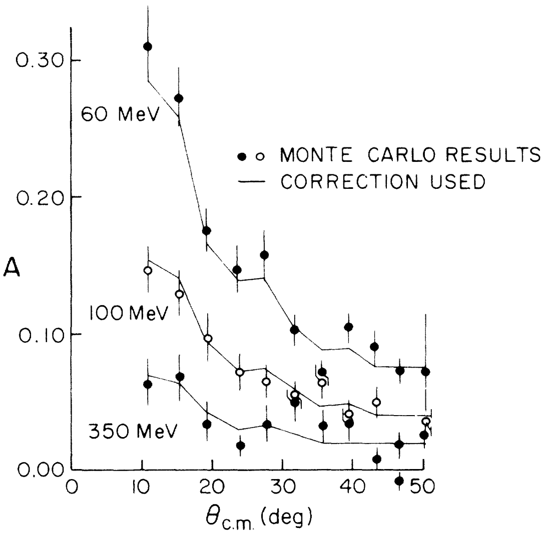

FIG. 13. Scattering corrections vs c.m. scattering angle determined by Monte Carlo calculation. The points are values produced by the program. The broken line is the parameterization of these results which was used in the analysis.

H. Thick-target and beam-attenuation corrections

The reduction of the beam intensity in the downstream portions of the LH_2 target by scattering in its upstream portions reduced the effective beam intensity and changed the normalization by a factor of

$$\frac{l}{\int_0^l e^{-px\sigma_t}\, dx} = \frac{pl\sigma_t}{(1 - e^{-pl\sigma_t})} \quad \left(\cong 1 + \frac{pl\sigma_t}{2} \right) ,$$

where σ_t is the n-p total cross section at the incident energy. This factor decreased monotonically with energy from 1.205 in the lowest energy bin to 1.050 in the highest. Since σ_t is accurately known[21] the uncertainty in this correction was negligible.

A further correction to the normalization was necessary due to the attenuation of the beam by material between the LH_2 target flask and the detector during beam runs. This correction factor was calculated from published n-nucleus total cross sections.[19] It varied from 0.93 in the lowest energy bin to 0.978 in the highest. Again, the accuracy of the total cross-section data made the uncertainty negligible.

V. RESULTS AND CONCLUSION

Laboratory differential cross sections were transformed to provide c.m. differential cross sections, $d\sigma/d\Omega$, as a function of $\theta_{\text{c.m.}}$, the c.m. scattering angle, and $d\sigma/d|t|$ as a function of momentum transfer in each energy bin. These results are presented in Table II and Fig. 14 as a function of the mean kinetic energy of neutrons detected in each energy bin in beam runs. The curves in Fig. 14 are the predictions of an energy-dependent phase-shift analysis of nearly all pre-

TABLE II. *np* forward differential cross sections.

E (mean) (MeV)	E (limits) (MeV)	$\theta_{\text{c.m.}}$ (deg)	$d\sigma/d\Omega$ (mb/sr)	$\lvert t\rvert$ [(GeV/c)^2]	$d\sigma/d\lvert t\rvert$ [mb/(GeV/c)^2]
58.8	54.6–63.1	11.8	15.13 ± 1.70	0.0012	1722 ± 193
		14.9	12.53 ± 0.64	0.0019	1426 ± 73
		19.0	13.55 ± 0.49	0.0030	1542 ± 55
		23.1	12.80 ± 0.49	0.0044	1456 ± 56
		27.1	12.12 ± 0.48	0.0060	1379 ± 55
		31.0	11.75 ± 0.63	0.0079	1337 ± 72
		34.8	11.98 ± 0.42	0.0099	1363 ± 48
		38.6	10.98 ± 0.53	0.0121	1250 ± 60
		42.3	11.27 ± 0.37	0.0144	1282 ± 43
67.5	63.1–72.1	11.9	9.88 ± 1.54	0.0014	979 ± 153
		15.0	12.03 ± 0.61	0.0021	1193 ± 61
		19.1	11.48 ± 0.45	0.0035	1138 ± 44
		23.1	11.89 ± 0.47	0.0051	1178 ± 47
		27.1	10.59 ± 0.44	0.0070	1049 ± 44
		31.1	10.53 ± 0.57	0.0091	1043 ± 57
		34.9	10.37 ± 0.38	0.0114	1028 ± 38
		38.7	8.94 ± 0.46	0.0139	886 ± 45
		42.4	9.71 ± 0.33	0.0166	963 ± 33
		46.0	8.40 ± 0.41	0.0194	833 ± 40
		49.5	6.92 ± 0.40	0.0222	686 ± 39
76.7	72.1–81.6	11.9	12.72 ± 1.42	0.0015	1108 ± 124
		15.0	10.89 ± 0.55	0.0025	949 ± 48
		19.1	10.49 ± 0.40	0.0040	915 ± 35
		23.2	9.88 ± 0.41	0.0058	861 ± 36
		27.2	9.59 ± 0.39	0.0080	836 ± 34
		31.1	8.87 ± 0.49	0.0104	773 ± 43
		35.0	8.94 ± 0.32	0.0130	779 ± 28
		38.8	7.45 ± 0.39	0.0159	649 ± 34
		42.5	7.98 ± 0.27	0.0189	696 ± 24
		46.1	6.72 ± 0.34	0.0221	586 ± 30
		49.6	5.63 ± 0.32	0.0254	491 ± 28
86.5	81.6–91.7	11.9	9.33 ± 1.31	0.0017	721 ± 102
		15.0	10.03 ± 0.53	0.0028	775 ± 41
		19.2	8.60 ± 0.37	0.0045	665 ± 29
		23.2	8.60 ± 0.38	0.0066	665 ± 29
		27.2	8.91 ± 0.36	0.0090	689 ± 28
		31.2	7.31 ± 0.45	0.0118	565 ± 35
		35.1	7.34 ± 0.29	0.0148	567 ± 22
		38.9	7.10 ± 0.36	0.0180	549 ± 28
		42.6	6.40 ± 0.25	0.0214	495 ± 19
		46.2	5.40 ± 0.30	0.0250	418 ± 23
		49.7	4.82 ± 0.30	0.0287	373 ± 23
96.8	91.7–102.2	11.9	9.47 ± 1.30	0.0020	654 ± 90
		15.1	9.33 ± 0.52	0.0031	644 ± 36
		19.2	8.26 ± 0.37	0.0051	571 ± 25
		23.3	8.49 ± 0.38	0.0074	587 ± 26
		27.3	8.53 ± 0.36	0.0101	590 ± 25
		31.3	7.13 ± 0.45	0.0132	492 ± 32
		35.2	7.36 ± 0.30	0.0166	509 ± 21
		39.0	6.13 ± 0.34	0.0202	423 ± 24
		42.7	6.17 ± 0.24	0.0241	426 ± 17
		46.3	4.92 ± 0.29	0.0281	340 ± 20
		49.8	4.75 ± 0.29	0.0323	329 ± 20

TABLE II. *(Continued)*

E (mean) (MeV)	E (limits) (MeV)	$\theta_{\text{c.m.}}$ (deg)	$d\sigma/d\Omega$ (mb/sr)	$\lvert t\rvert$ [(GeV/c)^2]	$d\sigma/d\lvert t\rvert$ [mb/(GeV/c)^2]
107.6	102.2–113.2	12.0	6.48 ± 1.28	0.0022	403 ± 80
		15.1	9.35 ± 0.51	0.0035	582 ± 32
		19.3	8.00 ± 0.37	0.0057	497 ± 23
		23.4	8.77 ± 0.38	0.0083	545 ± 24
		27.4	7.53 ± 0.35	0.0113	468 ± 22
		31.4	6.34 ± 0.43	0.0148	394 ± 27
		35.3	6.30 ± 0.28	0.0185	392 ± 17
		39.1	5.59 ± 0.34	0.0226	347 ± 21
		42.8	5.53 ± 0.23	0.0269	344 ± 15
		46.4	4.71 ± 0.29	0.0314	293 ± 18
		50.0	4.30 ± 0.28	0.0360	267 ± 18
118.8	113.2–124.8	12.0	8.72 ± 1.34	0.0024	491 ± 76
		15.2	8.84 ± 0.55	0.0039	498 ± 31
		19.3	7.13 ± 0.38	0.0063	401 ± 21
		23.4	7.39 ± 0.39	0.0092	416 ± 22
		27.5	6.63 ± 0.35	0.0126	373 ± 20
		31.4	6.03 ± 0.47	0.0164	340 ± 26
		35.3	6.19 ± 0.29	0.0206	348 ± 17
		39.2	5.25 ± 0.35	0.0251	295 ± 20
		42.9	4.83 ± 0.24	0.0299	272 ± 14
		46.5	4.76 ± 0.31	0.0348	268 ± 17
		50.1	3.28 ± 0.29	0.0400	184 ± 16
130.5	124.8–136.7	11.0	8.89 ± 0.42	0.0022	455 ± 22
		15.2	8.17 ± 0.25	0.0043	419 ± 13
		19.4	7.46 ± 0.19	0.0069	382 ± 10
		23.5	6.54 ± 0.20	0.0102	335 ± 10
		27.5	6.46 ± 0.37	0.0139	331 ± 19
		31.5	6.14 ± 0.46	0.0181	315 ± 23
		35.4	5.44 ± 0.29	0.0227	279 ± 15
		39.3	4.19 ± 0.36	0.0277	214 ± 19
		43.0	5.12 ± 0.26	0.0330	262 ± 13
		46.7	4.17 ± 0.32	0.0385	214 ± 16
		50.2	3.55 ± 0.30	0.0442	182 ± 16
142.8	136.7–149.1	11.0	8.48 ± 0.39	0.0025	397 ± 19
		15.2	7.66 ± 0.22	0.0047	359 ± 11
		19.4	7.05 ± 0.17	0.0076	330 ± 8
		23.6	6.55 ± 0.19	0.0112	307 ± 9
		27.6	6.10 ± 0.20	0.0153	286 ± 9
		31.6	5.16 ± 0.25	0.0199	242 ± 12
		35.5	5.03 ± 0.19	0.0250	236 ± 9
		39.4	4.70 ± 0.41	0.0304	220 ± 19
		43.1	4.25 ± 0.27	0.0362	199 ± 13
		46.8	3.70 ± 0.34	0.0423	173 ± 16
		50.3	3.68 ± 0.34	0.0485	173 ± 16
155.4	149.1–162.0	11.1	8.34 ± 0.39	0.0027	359 ± 17
		15.3	7.33 ± 0.23	0.0052	316 ± 10
		19.5	6.27 ± 0.17	0.0084	270 ± 7
		23.6	5.91 ± 0.19	0.0122	255 ± 8
		27.7	5.70 ± 0.20	0.0167	245 ± 8
		31.7	4.40 ± 0.23	0.0218	189 ± 10
		35.6	4.28 ± 0.19	0.0273	184 ± 8
		39.5	3.16 ± 0.27	0.0333	136 ± 12
		43.2	3.78 ± 0.18	0.0396	163 ± 8
		46.9	3.23 ± 0.22	0.0462	139 ± 10
		50.5	2.70 ± 0.22	0.0531	116 ± 9

TABLE II. *(Continued)*

E (mean) (MeV)	*E* (limits) (MeV)	$\theta_{\mathrm{c.m.}}$ (deg)	$d\sigma/d\Omega$ (mb/sr)	$\lvert t\rvert$ $[(\mathrm{GeV}/c)^2]$	$d\sigma/d\lvert t\rvert$ $[\mathrm{mb}/(\mathrm{GeV}/c)^2]$
168.5	162.0–175.2	11.1	7.59 ± 0.39	0.0030	301 ± 15
		15.3	6.89 ± 0.23	0.0056	274 ± 9
		19.5	5.83 ± 0.17	0.0091	231 ± 7
		23.7	5.61 ± 0.19	0.0133	222 ± 8
		27.8	4.97 ± 0.20	0.0182	198 ± 8
		31.8	4.35 ± 0.25	0.0238	173 ± 10
		35.8	4.08 ± 0.19	0.0298	162 ± 8
		39.6	2.92 ± 0.29	0.0363	116 ± 12
		43.4	3.45 ± 0.18	0.0432	137 ± 7
		47.0	3.05 ± 0.22	0.0504	121 ± 9
		50.6	2.49 ± 0.22	0.0578	99 ± 9
181.8	175.2–188.9	11.1	6.54 ± 0.39	0.0032	240 ± 14
		15.4	6.11 ± 0.23	0.0061	225 ± 8
		19.6	5.75 ± 0.18	0.0099	212 ± 7
		23.8	4.88 ± 0.19	0.0145	179 ± 7
		27.9	4.39 ± 0.20	0.0198	162 ± 7
		31.9	3.86 ± 0.25	0.0258	142 ± 9
		35.9	3.68 ± 0.20	0.0324	135 ± 7
		39.7	3.47 ± 0.31	0.0394	128 ± 11
		43.5	3.16 ± 0.20	0.0469	116 ± 7
		47.2	2.80 ± 0.22	0.0547	103 ± 8
		50.8	2.16 ± 0.22	0.0628	79 ± 8
195.6	188.9–202.9	11.2	7.48 ± 0.43	0.0035	255 ± 14
		15.4	6.10 ± 0.24	0.0066	209 ± 8
		19.7	5.18 ± 0.19	0.0107	177 ± 6
		23.9	4.98 ± 0.21	0.0157	170 ± 7
		28.0	4.43 ± 0.22	0.0215	151 ± 8
		32.0	3.95 ± 0.28	0.0279	135 ± 9
		36.0	3.67 ± 0.21	0.0351	126 ± 7
		39.9	3.16 ± 0.34	0.0427	108 ± 12
		43.6	3.59 ± 0.22	0.0508	123 ± 8
		47.3	2.57 ± 0.26	0.0592	88 ± 9
		50.9	2.11 ± 0.26	0.0679	72 ± 9
210.0	202.9–217.3	11.2	6.72 ± 0.46	0.0038	214 ± 15
		15.5	5.76 ± 0.26	0.0072	183 ± 8
		19.7	5.20 ± 0.21	0.0116	166 ± 7
		23.9	4.63 ± 0.23	0.0169	147 ± 7
		28.1	4.15 ± 0.24	0.0232	132 ± 8
		32.1	3.68 ± 0.30	0.0302	117 ± 10
		36.1	3.85 ± 0.25	0.0378	123 ± 8
		40.0	3.63 ± 0.38	0.0461	116 ± 12
		43.8	3.65 ± 0.25	0.0548	116 ± 8
		47.5	2.29 ± 0.30	0.0639	73 ± 10
		51.1	2.33 ± 0.30	0.0732	74 ± 10
224.3	217.3–232.1	11.2	6.39 ± 0.50	0.0040	191 ± 15
		15.5	6.06 ± 0.28	0.0077	180 ± 9
		19.8	5.18 ± 0.22	0.0125	154 ± 7
		24.0	4.82 ± 0.25	0.0182	144 ± 7
		28.2	4.22 ± 0.27	0.0249	126 ± 8
		32.2	4.13 ± 0.34	0.0325	123 ± 10
		36.2	3.19 ± 0.27	0.0407	95 ± 8
		40.1	3.40 ± 0.41	0.0496	101 ± 12
		43.9	3.16 ± 0.28	0.0589	94 ± 8
		47.6	2.26 ± 0.31	0.0687	67 ± 9
		51.2	2.67 ± 0.32	0.0788	80 ± 10

TABLE II. *(Continued)*

E (mean) (MeV)	E (limits) (MeV)	$\theta_{\text{c.m.}}$ (deg)	$d\sigma/d\Omega$ (mb/sr)	$\lvert t\rvert$ [$(\text{GeV}/c)^2$]	$d\sigma/d\lvert t\rvert$ [mb/$(\text{GeV}/c)^2$]
239.5	232.1–247.2	11.3	5.40 ± 0.52	0.0043	151 ± 15
		15.6	5.08 ± 0.30	0.0083	142 ± 8
		19.9	4.55 ± 0.24	0.0134	127 ± 7
		24.1	4.00 ± 0.27	0.0196	112 ± 8
		28.2	4.05 ± 0.31	0.0268	113 ± 9
		32.3	3.31 ± 0.36	0.0349	92 ± 10
		36.3	3.42 ± 0.30	0.0437	96 ± 8
		40.2	2.35 ± 0.47	0.0532	66 ± 13
		44.1	2.90 ± 0.31	0.0632	81 ± 9
		47.8	2.30 ± 0.38	0.0737	64 ± 11
		51.4	2.31 ± 0.38	0.0845	65 ± 11
267.2	247.2–294.4	11.4	6.75 ± 0.42	0.0050	167 ± 10
		15.7	5.27 ± 0.23	0.0095	130 ± 6
		20.0	4.42 ± 0.17	0.0153	109 ± 4
		24.3	4.15 ± 0.20	0.0224	103 ± 5
		28.4	3.89 ± 0.22	0.0307	96 ± 5
		32.6	3.61 ± 0.28	0.0399	89 ± 7
		36.6	3.31 ± 0.23	0.0500	82 ± 6
		40.5	2.82 ± 0.34	0.0609	70 ± 8
		44.3	3.38 ± 0.25	0.0724	83 ± 6
		48.1	2.73 ± 0.30	0.0843	67 ± 7
		51.7	2.47 ± 0.31	0.0966	61 ± 8
309.6	294.4–327.4	11.5	6.91 ± 0.73	0.0058	149 ± 16
		15.9	4.84 ± 0.37	0.0111	104 ± 8
		20.2	4.65 ± 0.30	0.0179	100 ± 6
		24.5	4.60 ± 0.34	0.0262	99 ± 7
		28.7	4.29 ± 0.39	0.0358	93 ± 8
		32.8	4.70 ± 0.50	0.0466	101 ± 11
		36.9	3.87 ± 0.41	0.0584	83 ± 9
		40.9	2.91 ± 0.64	0.0711	62 ± 14
		44.7	3.01 ± 0.45	0.0844	65 ± 10
		48.5	2.16 ± 0.51	0.0983	46 ± 11
		52.1	1.97 ± 0.53	0.1126	42 ± 11
343.8	327.4–361.5	11.6	5.86 ± 0.93	0.0065	114 ± 18
		16.0	5.60 ± 0.51	0.0125	109 ± 10
		20.3	4.83 ± 0.40	0.0202	94 ± 8
		24.7	3.64 ± 0.42	0.0295	71 ± 8
		28.9	3.77 ± 0.52	0.0403	73 ± 10
		33.1	3.28 ± 0.61	0.0524	64 ± 12
		37.2	3.32 ± 0.54	0.0656	65 ± 10
		41.1	1.74 ± 0.84	0.0798	34 ± 16
		45.0	2.95 ± 0.61	0.0947	57 ± 12
		48.8	1.75 ± 0.71	0.1103	34 ± 14
		52.5	2.29 ± 0.73	0.1263	44 ± 14
390.2	361.5–432.6	11.7	7.16 ± 0.98	0.0077	121 ± 16
		16.2	5.34 ± 0.52	0.0147	90 ± 9
		20.6	4.66 ± 0.40	0.0238	79 ± 7
		24.9	5.01 ± 0.47	0.0348	84 ± 8
		29.2	4.82 ± 0.52	0.0475	81 ± 9
		33.4	3.59 ± 0.66	0.0617	61 ± 11
		37.6	4.44 ± 0.53	0.0772	75 ± 9
		41.6	1.62 ± 0.88	0.0939	27 ± 15
		45.5	3.95 ± 0.68	0.1114	67 ± 11
		49.3	3.16 ± 0.75	0.1296	53 ± 13
		53.0	3.84 ± 0.86	0.1483	65 ± 15

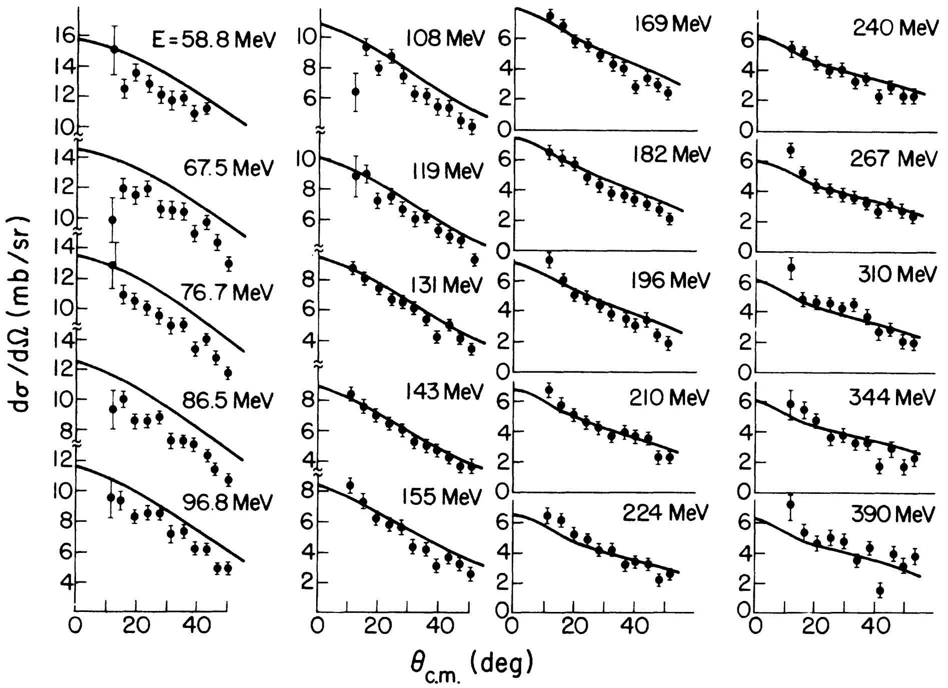

FIG. 14. Neutron-proton differential cross sections between 58.5 and 390 MeV. The curves are predictions of a phase-shift analysis.[14]

vious *N*-*N* scattering data between 1 and 450 MeV.[14]

The error bars in Fig. 14 and the quoted uncertainties of the individual points which are listed in Table II are those due to counting statistics. There were two other important sources of uncertainty which are not listed there because their effects were correlated with energy or scattering angle. The first was the 10% uncertainty in the normalization. This was dominated by the inconsistency in the beam runs (Sec. IV G) so deviations from the true normalization should be a smooth function of energy. Second was the uncertainty due to approximations made in the Monte Carlo calculation of the dependence of detector efficiency on scattering angle (Sec. IV E). These uncertainties vanish at 0° and increase quadratically with scattering angle to a maximum of 5% at 55° c.m.

Our results are generally consistent with the phase-shift predictions and with other experiments except for two features. First, the previous data below 130 MeV, virtually all of which are due to the Harwell experiment,[5] significantly higher than are our results. The phase-shift predictions are also higher than our results as might be expected, since they use the Harwell data. On the other hand, the phase-shift predictions are lower than the Harwell data and just within our uncertainties. Furthermore, phase-shift analysts[2] recently have suggested that the Harwell data are too high around 50 MeV since they are above those from the latest experiment[4] at that energy and their use yields values for $\delta(P_1)$ which are inconsistent with theoretical expectations. An energy-dependent analysis which includes our data may shed further light on these inconsistencies.

The second notable feature of the results is their forward peaking[22] at energies above 140 MeV. This peaking is consistent with some experiments[8,10] but it is stronger than that exhibited by the phase-shift predictions and it is inconsistent with the most forward data at 300 and 400 MeV.[11,13] Several of the latter data, however, were excluded from the Livermore data set[1] because they were very inconsistent with phase-shift fits to the remaining data. Here, too, an energy-dependent phase-shift analysis which includes our data should help clarify the situation.

ACKNOWLEDGMENTS

Thanks are due to the staff of the PPA, who provided unfailing support while data were being taken, and to M. Noble, L. Rudnick, and J. Dakin who assisted during various stages of the work.

*Work supported by the Atomic Energy Commission under Contract No. AT(11-1)-3072 [formerly AT(30-1)-4159] and Contract No. (W-7405-ENG-36) and the National Science Foundation under Grants No. NSF-GU-1592 and No. NSF-GP-14703.

† Present address: Physics Department, Rutgers—the State University, New Brunswick, New Jersey 08903.

‡ Present address: MP Division, Los Alamos Scientific Laboratory, Los Alamos, New Mexico 87544.

[1] M. H. MacGregor, R. A. Arndt, and R. M. Wright, Phys. Rev. 173, 1272 (1968).

[2] R. A. Arndt, J. Binstock, and R. Bryan, Phys. Rev. D 8, 1397 (1973).

[3] R. A. Arndt and L. D. Roper, Nucl. Phys. B50, 285 (1972).

[4] T. C. Montgomery, F. P. Brady, B. E. Bonner, W. B. Broste, and M. W. McNaughton, Phys. Rev. Lett. 31, 640 (1973).

[5] J. P. Scanlon, G. H. Stafford, J. J. Thresher, P. H. Bowen, and A. Langsford, Nucl. Phys. 41, 401 (1963).

[6] J. J. Thresher, R. G. P. Voss, and R. Wilson, Proc. R. Soc. London 229, 492 (1955).

[7] T. C. Randle, D. M. Skyrme, M. Snowden, A. E. Taylor, F. Uridge, and E. Wood, Proc. Phys. Soc. London 69, 760 (1956).

[8] Yu. M. Kazarinov and Yu. N. Simonov, Zh. Eksp. Teor. Fiz. 43, 35 (1962) [Sov. Phys.—JETP 16, 24 (1963)].

[9] E. Kelly, C. Keith, E. Segrè, and C. Wiegand, Phys. Rev. 79, 96 (1950).

[10] J. W. Easley, University of California Radiation Laboratory Report No UCRL-2693, 1954 (unpublished).

[11] J. De Pangher, Phys. Rev. 99, 1447 (1955).

[12] V. P. Dzhelepov and Yu. M. Kazarinov, Dokl. Akad. Nauk SSSR 99, 939 (1954).

[13] A. J. Hartzler, R. T. Siegel, and W. Opitz, Phys. Rev 95, 591 (1954).

[14] R. A. Arndt (private communication).

[15] M. W. Strovink, Princeton-Pennsylvania Accelerator Technical Note No. A-243, 1966 (unpublished).

[16] Neutron and K_L intensities were estimated from the p and K^+ intensities found by P. A. Piroué and A. J. S. Smith, Phys. Rev. 148, 1315 (1966). Neutron-proton inelastic cross sections were from the compilation in W. O. Lock and D. F. Measday, *Intermediate Energy Nuclear Physics* (Methuen, London, 1970), p. 199.

[17] J. T. Dakin, M. G. Hauser, M. M. Kreisler, and R. E. Mischke, Princeton University Elementary Particles Laboratory Technical Report No. 4, 1970 (unpublished).

[18] Inelastic n-nucleus interactions were approximated by simulating an intranuclear cascade of N-N interactions. Relative numbers of elastic and inelastic interactions used in this calculation were determined from the data of W. Schimmerling, T. J. Devlin, W. W. Johnson, K. G. Vosburgh, and R. E. Mischke, Phys. Rev. C 7, 248 (1973).

[19] Neutron-nucleus data for these calculations were derived from the following sources: P. Hillman, R. H. Stahl, and N. F. Ramsey, Phys. Rev. 96, 115 (1954); M. Arnold, P. E. Hodgson, D. F. Shaw, and D. M. Skyrme, Nucl. Phys. 19, 500 (1960); J. DeJuren, Phys. Rev. 80, 27 (1950); J. DeJuren and N. Knable, *ibid.* 77, 606 (1950); R. H. Hildebrand and C. E. Leith, *ibid.* 80, 842 (1950); M. Auman, F. P. Brady, J. A. Jungerman, W. J. Knox, M. R. McGie, and T. C. Montgomery, Phys. Rev. C 5, 1 (1972); R. Fox, C. Leith, L. Wouters, and K. R. MacKenzie, Phys. Rev. 80, 23 (1950); A. Ashmore, R. G. Jarvis, D. S. Mather, and S. K. Sen, Proc. Phys. Soc. London 70, 745 (1957); A. E. Taylor, T. G. Pickavance, J. M. Cassels, and T. C. Randle, Philos. Mag. 42, 751 (1951); R. Alphonce, J. Johansson, A. E. Taylor, and G. Tibell, *ibid.* 46, 295 (1955); A. E. Taylor and E. Wood, *ibid.* 44, 95 (1953); A. Bratenahl, S. Fernbach, R. H. Hildebrand, C. E. Leith, and B. J. Moyer, Phys. Rev. 77, 597 (1950); A. Ashmore, D. S. Mather, and S. K. Sen, Proc. Phys. Soc. London 71, 552 (1958); W. P. Ball, University of California Radiation Laboratory Report No. UCRL-1938, 1952 (unpublished); R. P. G. Voss and R. Wilson, Proc. R. Soc. London 236, 41 (1962); C. P. van Zyl, R. G. P. Voss, and R. Wilson, Philos. Mag. 1, 1003 (1956). G. L. Salmon, Nucl. Phys. 21, 15 (1960). Total cross sections were interpolated for use in scattering calculations. Inelastic cross sections were assumed independent of energy, as suggested by Voss and Wilson.

[20] Large-angle n-p cross sections were calculated from the phase shifts of Ref. 1 and M. H. MacGregor, R. A. Arndt, and R. M. Wright, Phys. Rev. 169, 1128 (1968). Small-angle cross sections were from Ref. 14.

[21] Total cross sections were obtained by interpolation of data in the compilation of R. Wilson, *The Nucleon-Nucleon Interaction* (Wiley, New York, 1963).

[22] For evidence of backward peaking see P. F. Shepard, T. J. Devlin, R. E. Mischke, and J. Solomon, Phys. Rev. D 10, 2735 (1974).